# The Konus-Wind observations of gamma-ray bursts with known redshifts

A. Tsvetkova*, D. Frederiks, D. Svinkin, S. Golenetskii, A. Lysenko, M. Ulanov, R. Aptekar

*Ioffe Institute, Politekhnicheskaya 26, St. Petersburg 194021, Russia; tsvetkova@mail.ioffe.ru*

**Abstract** We present the results of a systematic study of 166 gamma-ray bursts (GRBs) with reliable redshift estimates detected in the triggered mode of the Konus-Wind (KW) experiment. The sample covers the period from 1997 February to 2018 October and represents the largest set of cosmological GRBs studied to date over a broad energy band. For these bursts, we derived the durations, the spectral lags, the results of spectral fits with two model functions, the total energy fluences, and the peak energy fluxes, the rest-frame, isotropic-equivalent energy and peak luminosity, and the collimation-corrected values of the energetics for 32 GRBs with reasonably-constrained jet breaks. We consider the behavior of the rest-frame GRB parameters in the hardness-duration and hardness-intensity planes, and confirm the "Amati" and "Yonetoku" relations for Type II GRBs. The correction for the jet collimation does not improve these correlations for the KW sample. We discuss the influence of instrumental selection effects on the GRB parameter distributions and estimate the KW GRB detection horizon. Accounting for the instrumental bias, we estimate the KW GRB luminosity evolution, luminosity and isotropic-energy functions, and the evolution of the GRB formation rate.

**Keywords:** Gamma-Ray Bursts, Redshift

## 1. Instrumentation and the burst sample

KW is a gamma-ray spectrometer designed to study temporal and spectral characteristics of GRBs, solar flares, soft gamma repeater bursts, and other transient phenomena over a wide energy range from ~20 keV to ~10 MeV (at present). It consists of two identical omnidirectional NaI(Tl) detectors, mounted on opposite faces of the rotationally stabilized Wind spacecraft, which observe the entire celestial sphere. In interplanetary space far outside the Earth's magnetosphere, KW has the advantages over Earth-orbiting GRB monitors of continuous coverage, uninterrupted by Earth occultation, and a steady background, undistorted by passages through Earths trapped radiation, and subject only to occasional solar particle events. is expected that authors will submit carefully written and proofread material. Careful checking for spelling and grammatical errors should be performed.

The sample comprises 150 GRBs with reliable redshift estimates detected by KW in the triggered mode from the beginning of the afterglow era in 1997 to the middle of 2016 (Tsvetkova et al. 2017), supplemented by 16 GRBs detected by KW recently, and represents the largest set of cosmological GRBs studied to date over a broad energy band. Among these GRBs, 14 bursts (or 8%) belong to the Type I (merger origin, short/hard) GRB population and

the others are Type II (collapsar origin, long/soft) bursts (see Svinkin et al. (2016) for the KW GRB classification details).

## 2. Analyses and results

We derived the durations $T_{100}$, $T_{90}$, and $T_{50}$ (the total burst duration and the time intervals that contain 5% to 95% and 25% to 75% of the total burst count fluence, respectively), and the spectral lags, quantitative measures of spectral evolution often seen in long GRBs, when the emission in a soft detector band peaks later or has a longer decay relative to a hard band; a positive spectral lag corresponds to the delay of the softer emission. Figure 1 presents the $T_{50}$, $T_{90}$, and $T_{100}$ observer- and rest-frame distributions. We note that the observer-frame energy band 80–1200 keV, in which the durations are calculated, corresponds to multiple energy bands in the source-frame thus introducing a variable energy-dependant factor which must be accounted for when analyzing the rest-frame durations. The same considerations apply to the spectral lags.

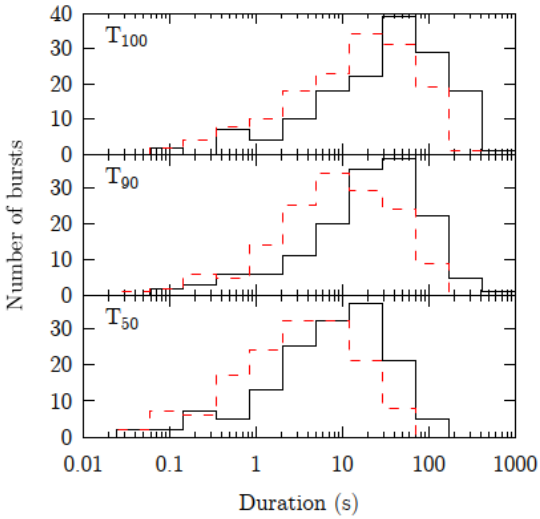


***Fig1.*** *Distributions of $T_{100}$ (top), $T_{90}$ (middle), and $T_{50}$ (bottom) in the observer- and cosmological rest frames (black solid and red dashed lines, respectively).*

For each burst from our sample, two time intervals were selected for spectral analysis: time-averaged fits were performed over the interval closest to $T_{100}$ (hereafter the TI spectrum); the peak spectrum corresponds to the time when the peak count rate (PCR) is reached. Each spectrum was fitted by two spectral models. The first model is the Band function (hereafter BAND; Band et al. 1993), and the second spectral model is an exponentially cutoff power-law (CPL). In the only case where both "curved" models result in ill-constrained fits (GRB 080413B), a simple power-law (PL) function was used. All the spectral models were normalized to the energy flux (F) in the 10 keV– 10 MeV range (observer frame). The best-fit spectral model (the BEST model) was chosen based on the difference in $\chi^2$ between the CPL and the BAND fits. The criterion for accepting a model with a single additional parameter is a

change in $\chi^2$ of at least 6 ($\Delta\chi^2 \equiv \chi^2_{CPL} - \chi^2_{BAND} > 6$). We found BAND to be the BEST model for 61 TI and 56 peak spectra. The remaining spectra (with the exception of GRB 080413B) were best fitted by CPL. Figure 2 shows the distributions of peak energies $E_{\rm p}$. The TI spectrum $E_{\rm p}$ ($E_{\rm p,i}$) distributions for both spectral models peak around 250 keV, while the peak spectrum $E_{\rm p}$ ($E_{\rm p,p}$) distributions peak around 300 keV.

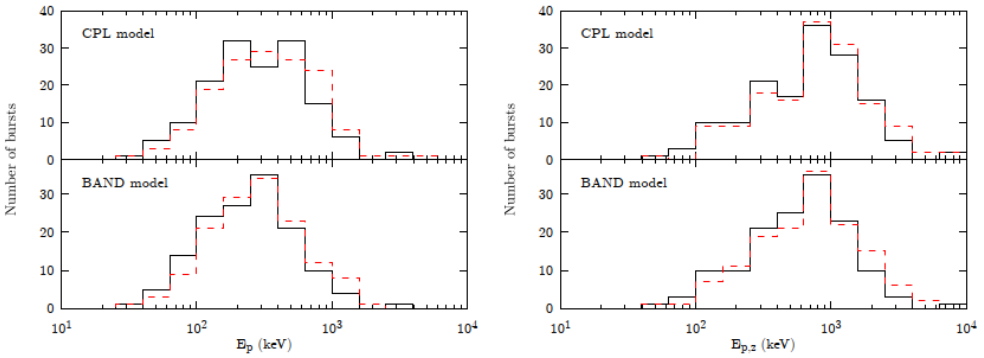


***Fig2.*** *Distributions of $E_p$, and $E_{p,z} = (1+z)E_p$. All the panels display the comparison between the TI spectral parameters (solid black lines) and the peak spectral parameters (dashed red lines), and the comparison between CPL and BAND spectral parameters.*

Figure 3 shows $E_{\rm p,i}$ as a function of the burst durations $T_{90}$ in the observer and rest frames. In the observer frame the KW Type I GRBs are typically harder and shorter than Type II bursts, which is consistent with the classification obtained from the hardness-duration distribution, and this tendency shows no dependence on the burst redshift. In the cosmological rest frame this pattern remains practically unchanged for GRBs at $z \lesssim 1.7$ but it appears to be less distinct when the whole sample is considered. Although in the rest frame Type I GRBs are still shorter

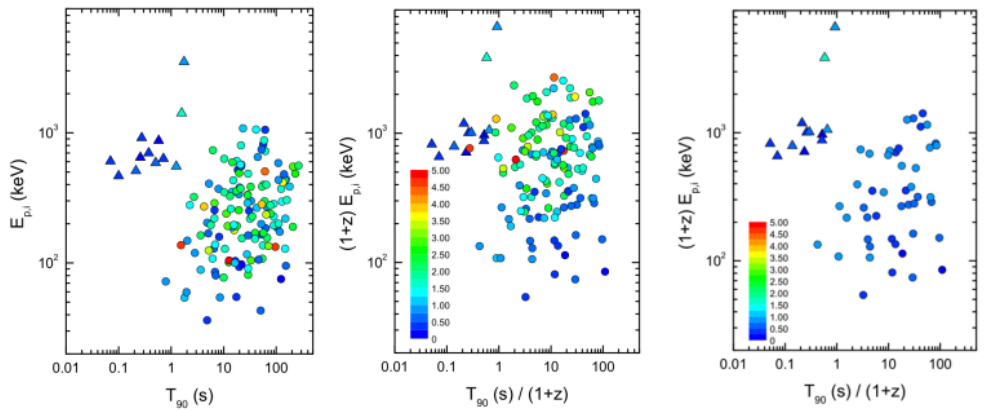


***Fig3.*** *$E_{p,i}$ – $T_{90}$ diagram in the observer (left panel) and rest (central and right panels) frames. The Type II GRBs with z> 1 are excluded from the sample shown on the right panel. The color of each data point (Type I: triangles, Type II: circles) represents the burst redshift.*

than Type II GRBs, their rest-frame $E_p$, clustered around 1 MeV, are superseded by those of a

significant fraction of the Type II population. We note, however, that the derived rest-frame durations are affected by a variable energy-dependant factor and the KW rest-frame $E_p$ are subject to the observational bias thus an interpretation of the rest-frame hardness-duration distribution should be done with care.

From the BEST spectral models we calculated the 10 keV–10 MeV energy fluences ($S$) and the peak energy fluxes ($F$peak) on three time scales: 1024 ms, 64 ms, and (1 + $z$)64 ms (the GRB rest-frame 64 ms scale). Based on the GRB redshifts, which span the range $0.1 \leq z \leq 5$, we estimated the rest-frame, isotropic-equivalent energies ($E_{iso}$) and peak luminosities ($L_{iso}$) in the rest-frame bolometric range 1 keV–(1 + $z$)10 MeV. For 32 GRBs with reasonably constrained jet break times ($t_{jet}$) we derived the collimation-corrected values of the energetics.

## 3. KW selection effects and GRB detection horizon

Figure 4 shows the KW GRB distributions in the $z$–$E_{iso}$, $z$–$L_{iso}$, and $z$–$E_{p,z}$ diagrams[1]. The region in the $z$–$L_{iso}$ plane above the limit defined by the bolometric flux $F_{lim} \sim 1\times10^{-6}$ erg cm$^{-2}$ s$^{-1}$ may be considered free from the selection bias. In the $z$–$E_{iso}$ plane, the selection-free region corresponds to the bolometric fluence $S_{lim} \gtrsim 3 \times 10^{-6}$ erg cm$^{-2}$. The detector sensitivity drops rapidly as $E$p (the peak energy in $\nu F_\nu$ spectrum) approaches the lower boundary of the KW band, and this results in a lack of bursts below the rest-frame limit $\approx (1+z)^2 \cdot 25$ keV in the $z$ - $E_{p,z}$ plane.

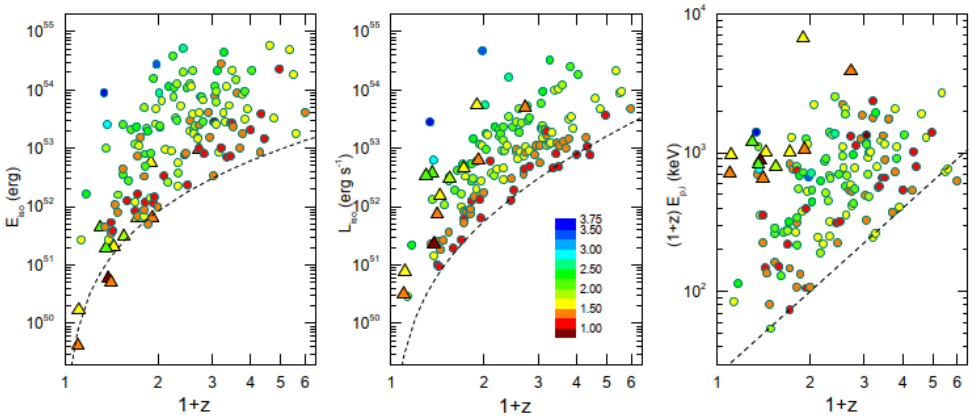


***Fig4.*** *KW GRB $E_{iso}$, $L_{iso}$, and $E_{p,i,z}$ vs. redshift. The color of each data point (Type I: triangles, Type II: circles) represents the log of the burst's trigger significance (□). The observer-frame limits are shown with dashed lines.*

Accounting for the KW trigger sensitivity to the GRB incident angle, its light-curve shape, and the shape of the energy spectrum, we estimated the KW detection horizon for each burst from the sample as a redshift $z_{max}$, at which the GRB peak count rate in the trigger energy band (~80–300 keV) drops below the trigger threshold (9$\sigma$) on both trigger time scales (140 ms and 1 s). The most distant GRB horizon for the KW sample ($z_{max} \approx 16.6$) is reached for the ultra-luminous GRB 110918A (Frederiks et al. 2013) at observed $z = 0.981$. At $z \approx 16.6$ the age

[1] We use $A_z$ notation for rest-frame GRB parameters.

of the Universe amounts to only ~ 230 Myr, i.e. a burst which occurred close to the end of the cosmic Dark Ages could still trigger the KW detectors, and a thorough temporal and spectral analysis in a wide observer-frame energy range could be performed.

A common approach to estimate the GRB detection horizon is to find a redshift $z_{\rm max,L}$, at which the limiting isotropic luminosity $L_{\rm iso,lim} = 4\pi\, D_{\rm L}^{\,2} \times F_{\rm lim}$, defined by the "monolithic" $F_{\rm lim}$ estimated for the whole sample, starts to exceed the GRB $L_{\rm iso}$. We found that for both Type I and Type II GRBs $z_{\rm max}$ are distributed narrowly around $z_{\rm max,L}$ corresponding to the bolometric $F_{\rm lim} = 1 \times 10^{-6}$ erg cm$^{-2}$ s$^{-1}$.

## 4. GRB Luminosity and Isotropic-energy functions, GRB Formation Rate

To estimate the GRB luminosity function (LF), isotropic energy release function (EF), and the cosmic GRB formation rate (GRBFR) for the KW Type II bursts we used the non-parametric Lynden-Bell $C^-$ method (Lynden-Bell 1971) further advanced by Efron & Petrosian (1992) (the EP method); the details of our calculations are described in Tsvetkova et al. (2017). Applying the EP method to the $z$–$L_{\rm iso}$ plane and using the functional form of the evolution $(z) = (1 + z)$, we found the luminosity evolution significance $\tau_0 \sim 1.7\sigma$, and estimated the luminosity evolution index $\delta_L = 1.7^{+0.9}_{-0.9}$. Applying the same method to the $z$–$E_{\rm iso}$ plane, we found $\delta_E = 1.1^{+1.5}_{-0.7}$ ($\tau_0 \sim 1.6\sigma$). Thus, the estimated $E_{\rm iso}$ and $L_{\rm iso}$ evolutions are comparable.

Then, using the $C^-$ method, we obtained evolution-free cumulative LF and EF, $\psi(L')$ and $\psi(E')$ (Figure 5), where $L' = L_{\rm iso}/(1 + z)^{\delta L}$ and $E' = E_{\rm iso}/(1 + z)^{\delta E}$, and fitted the distributions with a broken power-law (BPL) function and with the exponentially-cutoff PL (CPL). The derived BPL slopes of LF and EF are close to each other, both for the dim ($\alpha_1 \sim -0.5$) and bright ($\alpha_2 \sim -1$) segments; also, these indices are roughly consistent with the LF and EF slopes obtained in Yonetoku et al. (2004) and Wu et al. (2012). When compared to BPL, the CPL fit to $(L')$ results in a considerably worse quality. Conversely, the cutoff PL fits $(E')$ better ($\Delta\chi^2 \sim 5.5$), with the PL slope ~ −0.35 and the cutoff energy $E'_{\rm cut} \gtrsim 10^{54}$ erg. The existence of a sharp cutoff of the GRB isotropic energy distribution around $\sim 1 - 3 \times 10^{54}$ erg was suggested recently by Atteia et al. (2017). We also estimated the LF and EF not accounting for the evolution, and found them very similar in shape to $(L')$ and $(E')$.

The GRBFR (Figure 5), estimated using the EP method from the evolution-corrected $z$– $L'$ distribution, exceeds the star formation rate (SFR) at $z < 1$ and nearly traces the SFR at higher redshifts; the same behavior is noted for the GRBFRs estimated using both the evolution-corrected $z$-$E'$ and the non-corrected $z$-$E_{\rm iso}$ distributions. The low-$z$ GRBFR excess over SFR is in agreement with the results reported in Yu et al. (2015) and Petrosian et al. (2015). Meanwhile, the only GRBFR that traces the SFR in the whole KW GRB redshift range is the one derived from the $z$–$L_{\rm iso}$ distribution (i.e. not accounting for the luminosity evolution).

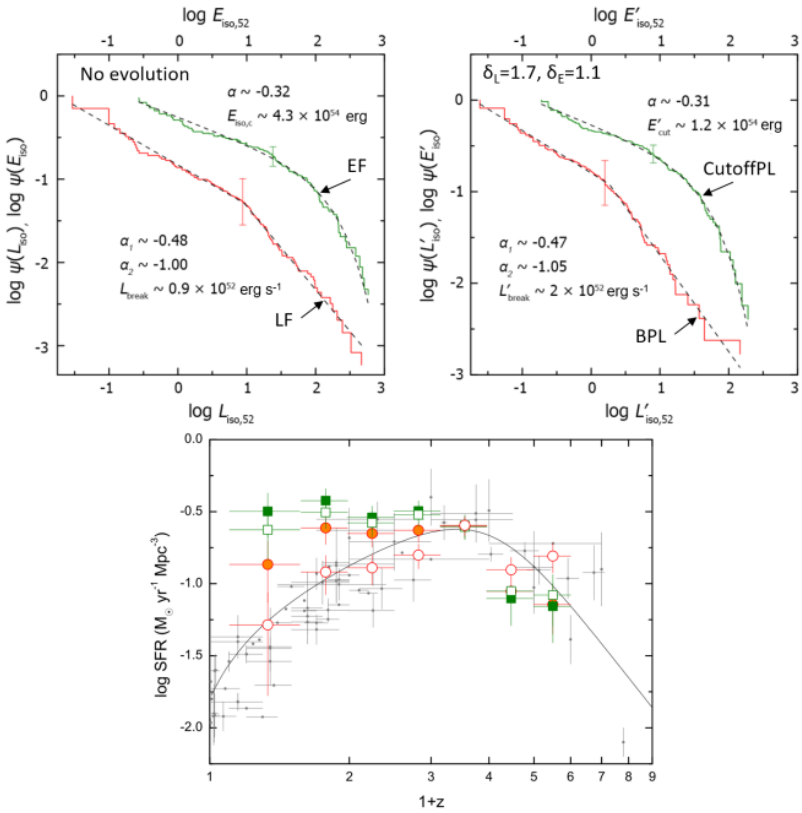


***Fig5.*** *Top: cumulative LF (red stepped graph) and EF (green stepped graph) estimated accounting for the luminosity and energy evolutions; the solid and dashed lines show the best BPL and CPL fits, respectively. Bottom: GRBFR calculated using four datasets: z-$L_{iso}$ (no luminosity evolution, red open circles), z-L′ ($\delta_L$ = 1.7, red filled circles), z-$E_{iso}$ (no energy evolution, green open squares), and z-E′ ($\delta_E$ = 1.1, green filled squares). The gray points and the solid line show the SFR data from the literature (for references see Tsvetkova et al. 2017). The GRBFR points have been shifted arbitrarily to match the SFR at (1 + z) ~ 3.5.*

## 5. Hardness-intensity correlations

We tested the KW GRB characteristics against $E_p$–$S$ and $E_p$–$F_{peak}$ correlations in the observer frame, and $E$p,z–$E$iso (“Amati”, Amati et al. 2002) and $E_{p,z}$–$L_{iso}$ (“Yonetoku”, Yonetoku et al. 2004) correlations in the rest frame. For the subsamples of Type I and Type II KW GRBs both the Amati and Yonetoku correlations improve considerably when moving from the observer frame to the GRB rest frame, with only marginal changes in the slopes. The derived slopes of the Amati and Yonetoku relations for Type II GRBs are ~0.47 and ~0.49, respectively. These values are in agreement with Amati et al. (2002), Yonetoku et al. (2004). For 30 KW Type II GRBs with reliable $t_{jet}$, accounting for the jet collimation neither improves the significance of the correlations nor reduces the dispersion of the points around the best-fit relations. The slopes we obtained for the collimated Amati and Yonetoku relations are steeper compared to those of the non-collimated versions.

The lower boundaries of both the Amati and Yonetoku relations (Figure 6) are defined by

GRBs with moderate-to-high detection significance, so the instrumental biases do not affect the correlations from this edge of the distributions. Meanwhile, all outliers in the relations lie *above* the upper boundaries of the 90% prediction intervals (PIs) of the relations. Since these bursts were detected at lower significance, with the increased number of GRB redshift observations, one could expect a "smear" of the correlations due to more hard-spectrum/less-energetic GRB detections. Thus, using the KW sample, we confirm a finding of Heussaff et al. (2013) that the lower right boundary of the Amati correlation (the lack of luminous soft GRBs) is an intrinsic GRB property, while the top left boundary may be due to selection effects. For the KW sample, this conclusion may also be extended to the Yonetoku correlation.

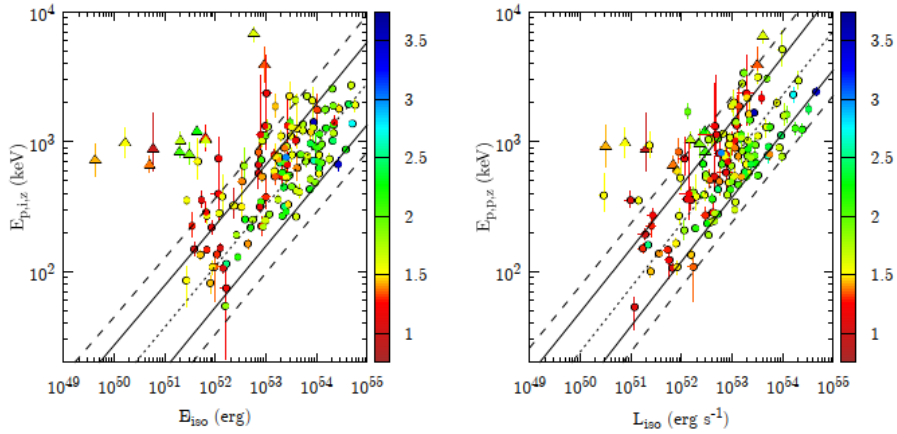


***Fig6.*** *Rest-frame energetics in the $E_{iso} - E_{p,z}$ (left) and $L_{iso} - E_{p,z}$ (right) planes. The color of each data point (Type I: triangles, Type II: circles) represents the log of the burst's trigger significance. The "Amati" and "Yonetoku" relations for Type II GRBs are plotted with dotted lines; the solid and dashed lines show their 68% and 90% PI's, respectively.*

The $E_{p,z}$–$E_{iso}$ and $E_{p,z}$–$L_{iso}$ correlations for the Type I bursts are less significant when compared to those for Type II GRBs, and they are characterized by less steep slopes. Meanwhile, the rest-frame $E_p$ of Type I GRBs shows only a weak (if any) dependence on the burst energy below $E_{iso} \sim 10^{52}$ erg (Figure 6), and the same is true for the $E_{p,z}$–$L_{iso}$ relation at $L_{iso} \lesssim 5\times10^{52}$ erg $s^{-1}$. Above these limits the slopes of both relations for Type I GRBs are similar to those for Type II GRBs. As one can see from the Figure, all KW Type I bursts are hard-spectrum/low-isotropic- energy outliers in the Amati relation for Type II GRBs. In the $E_{p,z}$–$L_{iso}$ plane this pattern is less distinct; at luminosities above $L_{iso} \sim 10^{52}$ erg $s^{-1}$ the Type I bursts nearly follow the upper boundary of the Type II GRB Yonetoku relation.

## 6. Conclusions

We hope this work will encourage further investigations of GRB physical properties and will contribute to other related studies. Plots of the GRB light curves and spectral fits can be found at the Ioffe Web site[2]. This work was supported by RSF (grant 17-12-01378).

[2] http://www.ioffe.ru/LEA/zGRBs/triggered/

## References


[1] Amati, L., Frontera, F., Tavani, M., et al. 2002, A&A, **390**, 81

[2] Atteia, J.-L., Heussaff, V., Dezalay, J.-P., et al. 2017, ApJ, **837**, 119

[3] Band, D., Matteson, J., Ford, L., et al. 1993, ApJ, **413**, 281

[4] Efron, B., & Petrosian, V. 1992, ApJ, **399**, 345

[5] Frederiks, D. D., Hurley, K., Svinkin, D. S., et al. 2013, ApJ, **779**, 151

[6] Heussaff, V., Atteia, J.-L., & Zolnierowski, Y. 2013, A&A, **557**, A100

[7] Lynden-Bell, D. 1971, MNRAS, **155**, 95

[8] Petrosian, V., Kitanidis, E., & Kocevski, D. 2015, ApJ, **806**, 44

[9] Svinkin, D. S., Frederiks, D. D., Aptekar, R. L., et al. 2016, ApJS, **224**, 10

[10] Tsvetkova, A., Frederiks, D., Golenetskii, S., et al. 2017, ApJ, **850**, 161

[11] Wu, S.-W., Xu, D., Zhang, F.-W., & Wei, D.-M. 2012, MNRAS, **423**, 2627

[12] Yonetoku, D., Murakami, T., Nakamura, T., et al. 2004, ApJ, **609**, 935

[13] Yu, H., Wang, F. Y., Dai, Z. G., & Cheng, K. S. 2015, ApJS, **218**, 13